RAA 2017 Vol. **17** No. **12**, 126(12pp) doi: 10.1088/1674–4527/17/12/126

http://www.raa-journal.org *http://iopscience.iop.org/raa*

***R**esearch in*
***A**stronomy and*
***A**strophysics*

Is the filamentary dark cloud GF 6 a star forming region? — Stability analysis and infrared properties

Jaeheon Kim[1], Hyun-Goo Kim[2], Sang Joon Kim[3] and Bo Zhang[1]

[1] Shanghai Astronomical Observatory, Chinese Academy of Sciences, Shanghai 200030, China; *jhkim@shao.ac.cn*
[2] Korea Astronomy and Space Science Institute, Daejeon 34055, Korea
[3] Department of Astronomy and Space Science, Kyung Hee University, Yongin 17104, Korea

Received 2017 May 23; accepted 2017 September 21

Abstract We present the results of mapping observations and stability analyses toward the filamentary dark cloud GF 6. We investigate the internal structures of a typical filamentary dark cloud GF 6 to know whether the filamentary dark cloud will form stars. We perform radio observations with both ^{12}CO (J=1–0) and ^{13}CO (J=1–0) emission lines to examine the mass distribution and its evolutionary status. The ^{13}CO gas column density map shows eight subclumps in the GF 6 region with sizes on a sub-pc scale. The resulting local thermodynamic equilibrium masses of all the subclumps are too low to form stars against the turbulent dissipation. We also investigate the properties of embedded infrared point sources to know whether they are newly formed stars. The infrared properties also indicate that these point sources are not related to star forming activities associated with GF 6. Both radio and infrared properties indicate that the filamentary dark cloud GF 6 is too light to contract gravitationally and will eventually be dissipated away.

Key words: ISM: clouds — ISM: molecules — radio lines: ISM — infrared: ISM — Instabilities — Turbulence

1 INTRODUCTION

Globule-like small dark clouds (e.g. Bok globules) are well known as possible sites of low-mass star formation (Bok & Reilly 1947; Yun & Clemens 1990; Kirk et al. 2005). Many of these clouds are aligned with elongated or filamentary structures. These elongated-type objects are called Filamentary Dark Clouds or Globular Filaments (GFs), which often consist of several dense cores connected by a lower density region (Schneider & Elmegreen 1979; Larson 1985). Low-mass single or binary stars commonly develop in dense cores within molecular clouds, being aligned with large and complex filamentary structures (Benson & Myers 1989; di Francesco et al. 2007; André et al. 2014).

For individual filamentary dark clouds, including globules, several authors recently conducted multi-wavelength observations (Moreira & Yun 2002; Lehtinen et al. 2005; Samal et al. 2007; Stutz et al. 2010; Haikala & Reipurth 2010, 2017) and numerical simulations (Keto & Burkert 2014; Heigl et al. 2016 and references therein). As many authors proposed, we also expect that the lower density region (the filamentary substructure) in the GF may expand and disappear, whereas the higher density subclump (dense core) may contract and form a low-mass protostar. However, the origin and evolutionary status of the GFs are still not understood well. They normally have an extended shape, are less massive than isolated dark globules and can easily be dissociated by interstellar ultraviolet radiation. Therefore, it would be interesting to study the dynamical state and final destiny of GFs.

The filamentary dark cloud GF 6 (Schneider & Elmegreen 1979) is a small, elongated and arc-shaped dark cloud consisting of several subclumps and not far from the Sun. At optical wavelengths, this object seems to be made up of three subclumps of similar sizes. Figure 1 shows the Digitized Sky Survey (DSS) image of GF 6 ($\alpha_{\rm J2000} = 19^{\rm h}\ 01^{\rm m}\ 54.00^{\rm s}$, $\delta_{\rm J2000} = -05^\circ\ 31'\ 00''$), which extends over $3^\circ \times 2.4^\circ$. The three

subclumps are named B129, 127 and 130 in the catalog of Barnard (1927) or L549, 544 and 542 in the catalog of Lynds (1962) from the upper to lower ones, respectively. Clemens & Barvainis (1988) classified GF 6 as five individual globules (CB175, 172, 170, 173 and 174) from the upper to lower ones. These subclumps are connected to each other by a diffuse, less dense region. Therefore, this source may be a good example for studying the origin and dynamical status of a filamentary cloud. The rectangular box of Figure 1 outlines the area actually observed in the ^{13}CO (J=1–0) transition. In this paper, we present the gas column density map obtained from observations of ^{12}CO (J=1–0) and ^{13}CO (J=1–0) emission lines. From the column density distribution, we delineate several clumps and apply stability analysis to examine the evolutionary status for each clump. The dynamical properties between the clumps are also shown using the channel maps. We also investigate the infrared properties of the embedded infrared point sources identified by *IRAS* and *MSX* data.

In Section 2, we describe observations and their results, including the stability analysis. In Section 3, the infrared data and their properties are presented. The summary and conclusion are given in Section 4.

2 OBSERVATIONS AND THEIR RESULTS

2.1 CO Observations

Observations of the ^{12}CO (J=1–0, 115.2712 GHz) and ^{13}CO (J=1–0, 110.2014 GHz) lines were carried out using the 14-m radio telescope of the Taeduk Radio Astronomy Observatory (TRAO) administered by the Korea Astronomy and Space Science Institute (KASI). These observations were performed before the receiver system of the TRAO telescope was upgraded to a 16-beam receiver (SEQUOIA) system. The full mapping observation was made in the transition line of ^{13}CO (J=1–0), whereas the cross-scan observation was only performed in the ^{12}CO (J=1–0) line. The TRAO 14-m radio telescope and its instrumentation were described in detail by Kim & Jung (1992) and Roh & Jung (1999). The half-power beam width (HPBW) of the TRAO 14-m radio telescope is approximately $50''$ at the rest frequency of the ^{13}CO (J=1–0) line. The Superconductor-Insulator-Superconductor (SIS) receiver, equipped with a single-side band (SSB) filter, was used for the front end. For the back end, the 256-channel filter bank with a resolution of 250 kHz and the 1024 channel autocorrelator with a resolution of 20 kHz were used. The corresponding velocity resolutions of the filter bank and the autocorrelator are 0.65 and 0.054 km s^{-1}, respectively. The system noise temperature of the SSB ranged from 400 K to 500 K during observation of the ^{13}CO (J=1–0) line.

During the mapping observation, the telescope was pointed periodically at the center and reference positions. We obtained a mosaic of 625 positions over a $25' \times 25'$ region with $1'$ spacing. Antenna temperatures were corrected for atmospheric extinction and the forward spillover/scattering losses of the antenna and radome ($\eta_{\rm fss}$ = 0.63 at 110–115 GHz) were therefore estimated as the radiation temperature, $T_{\rm R}^{*}$, defined by Kutner & Ulich (1981). The root mean square (rms) noise level of the resulting spectra was less than approximately 0.3 K.

2.2 Cloud Morphology

The resulting map of the ^{13}CO (J=1–0) integrated intensity is presented in Figure 2. The starting contour is 0.6 K km s^{-1} and the contour increment is 0.5 K km s^{-1}. The scale of the color bar is in units of K km s^{-1}. From Figure 2, we identify eight subclumps in the GF 6 region. We mark them as GF 6-a, -b, -c, -d, -e and -f from the upper to the lower one and as GF 6-g and -h from the center to the left one, respectively.

In Table 1, we give information on the identified subclumps. Columns (1) to (3) list the identification number, defined name and other cataloged name, respectively. Columns (4) and (5) give the location of subclumps in right ascension (R.A.) and declination (Dec.), respectively. Columns (6) and (7) give the corrected radiation temperature and velocity centroid of ^{13}CO (J=1–0) emission at the peak position, respectively. The position and shape of the CO contour in Figure 2 seem to agree well with those of the high extinction region in Figure 1.

To see the velocity structures of the GF 6 region, we present channel maps integrated over a range of velocity bins. The channel maps at individual velocity spans are shown in Figure 3. Most emission appears at $V_{\rm LSR}$ from 9.6 to 11.2 km s^{-1}. The velocity coverage of each map is 0.16 km s^{-1}, which corresponds to three channels of the 20 kHz autocorrelator. The central $V_{\rm LSR}$ is shown in the upper right corner of each panel. Only $V_{\rm LSR}$ = 9.24 km s^{-1} to 11.63 km s^{-1} is presented in this figure, as no emission is found in the rest of the velocity range. The CO emission toward the GF 6 region is generally weak, and the lowest contour of Figure 3 is set to 0.6 K km s^{-1} ($\sim 3\sigma$). According to the velocity centroid, the subclumps can be divided into two groups. One is the

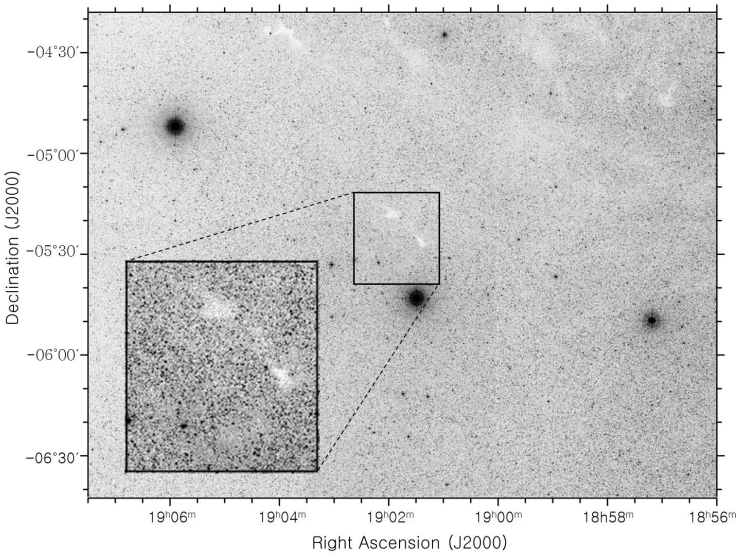

Fig. 1 The DSS image of the filamentary dark cloud GF 6, which extends over $3^\circ \times 2.4^\circ$.

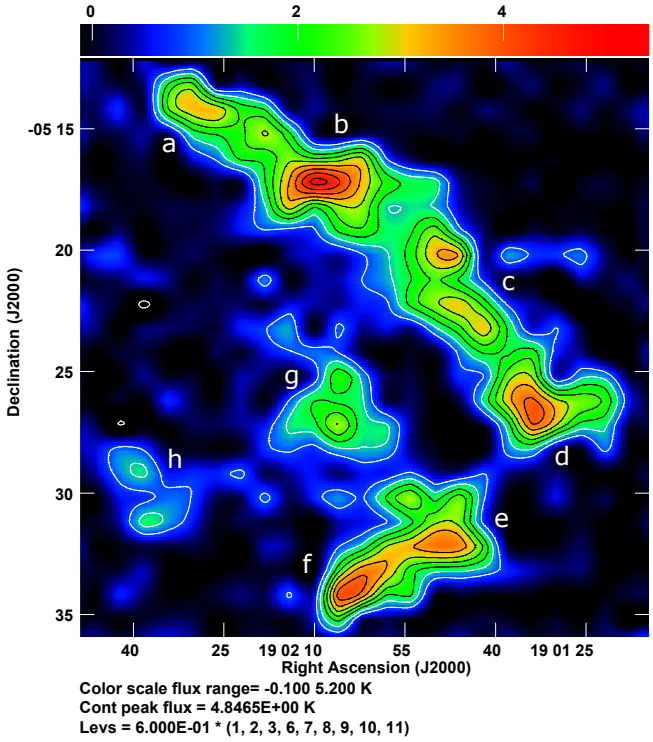

Fig. 2 The ^{13}CO (J=1–0) integrated intensity map. See the main text for the detailed description.

group of GF 6-a, -b, -c, -d and -h, which have an average $V_{\rm LSR}$ of 10.2 km s^{-1}; the other is the group of GF 6-e, -f and -g, with an average $V_{\rm LSR}$ of 10.7 km s^{-1}. The whole cloud of GF 6 looks similar to an arc-shaped expanding shell caused by a stellar wind from the center (the vicinity of GF 6-g).

2.3 Physical Properties

From ^{12}CO (J=1–0) and ^{13}CO (J=1–0) line observations, we derived various physical properties of individual subclumps, such as the ^{13}CO column densities, sizes, masses and the velocity distribution, by using the assumption of local thermodynamic equilibrium (LTE)

Table 1 Subclumps of GF 6

No.	Defined name	Other name	R.A. (J2000) (h m s)	Dec. (J2000) (d m s)	$T_{\rm R}^{*}(^{13}{\rm CO})_{\rm peak}$ (K)	$V_{\rm LSR}$ (km s^{-1})
(1)	(2)	(3)	(4)	(5)	(6)	(7)
1	GF 6-a	CB175, B129, L549	19 02 27	−05 15 40	1.73	10.1
2	GF 6-b	CB175, B129, L549	19 02 08	−05 18 01	3.03	10.1
3	GF 6-c	CB172	19 01 45	−05 21 44	2.52	10.1
4	GF 6-d	CB170, B127, L544	19 01 32	−05 27 20	3.73	10.2
5	GF 6-e	CB173, B130, L542	19 01 46	−05 32 51	3.51	10.7
6	GF 6-f	CB174, B130, L542	19 02 04	−05 34 50	3.80	10.6
7	GF 6-g	···	19 02 06	−05 27 50	1.78	10.8
8	GF 6-h	···	19 02 38	−05 30 58	2.13	10.3

Notes: CB – Clemens & Barvainis (1988), B – Barnard (1927), L – Lynds (1962).

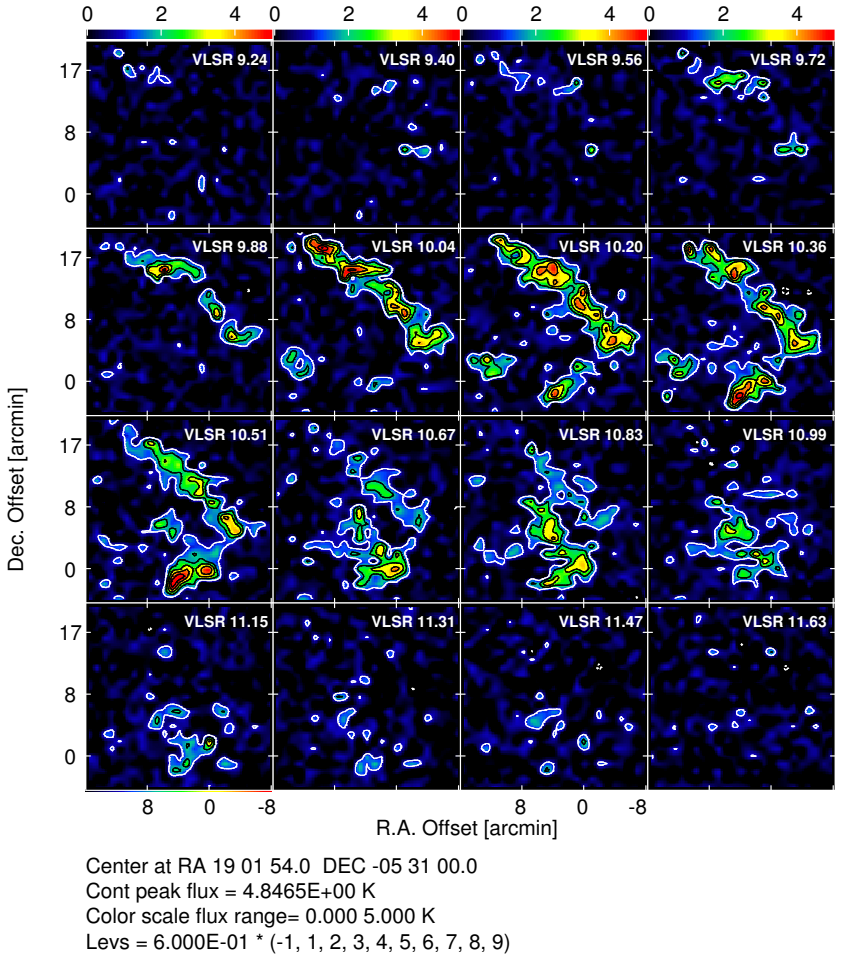

Fig. 3 The channel maps of the whole region. See the main text for a detailed description.

(Dickman 1978; Kim & Hong 2002). The radiation temperature $^{13}T_{\rm R}(v_{\rm i})$ at each channel $v_{\rm i}$ of the ^{13}CO (J=1–0) line is related to the excitation temperature $T_{\rm ex}$ and the cosmic background temperature $T_{\rm bg}$ as

$$^{13}T_{\rm R}(v_{\rm i}) = [J(\nu_{13}, T_{\rm ex}) - J(\nu_{13}, T_{\rm bg})] \times [1 - \exp(-^{13}\tau_{\rm i})], \quad (1)$$

where $J(\nu, T)$ (= $(h\nu/k)$ / $[\exp(h\nu/kT) - 1]$) represents the intensity in units of temperature (= effective radia-

tion temperature), ν_{13} is the rest frequency of the ^{13}CO (J=1–0) line and $^{13}\tau_{\rm i}$ is the optical depth of the line at the i-th channel. Since the ^{12}CO line is optically thick, Equation (1) simply becomes

$$^{12}T_{\rm R}(v_{\rm i}) = [J(\nu_{12}, T_{\rm ex}) - J(\nu_{12}, T_{\rm bg})]. \quad (2)$$

Equation (2) gives us $T_{\rm ex}$ as

$$T_{\rm ex}\,[{\rm K}] = 5.53 \left[\ln\left\{1 + \frac{5.53}{^{12}T_{\rm R}(v_0) + 0.84}\right\}\right]^{-1}, \quad (3)$$

where v_0 denotes the line center velocity. The radiation temperature $T_{\rm R}$ is estimated from the corrected antenna temperature $T_{\rm A}^*$ by the relation $T_{\rm R} = T_{\rm A}^* / \eta_{\rm fss}$. Assuming that the excitation temperature is the same for ^{12}CO and ^{13}CO transitions, we make use of Equation (1) and determine $^{13}\tau_{\rm i}$;

$$^{13}\tau_{\rm i} = -\ln\left[1 - {}^{13}T_{\rm R}(v_{\rm i}) \left\{\frac{5.29}{\exp(5.29/T_{\rm ex}) - 1} - 0.89\right\}^{-1}\right]. \quad (4)$$

The ^{13}CO column density within each channel is related to the optical depth and width of the channel by

$$\int {}^{13}\tau_{\rm i}(\nu)\, d\nu = \frac{8\pi^3\mu^2\,\nu_{13}}{3hc} \left[1 - \exp\left(-\frac{h\nu_{13}}{kT_{\rm ex}}\right)\right] \frac{N_{\rm i}(^{13}{\rm CO})}{Q}, \quad (5)$$

where μ (= 0.112 Debyes) is the permanent electric dipole moment for the CO molecule. The rotational partition function Q is approximated as $2kT_{\rm ex}\,/\,h\nu_{13}$. In terms of the observable quantities, the column density of ^{13}CO within a channel i is expressed by

$$N_{\rm i}(^{13}{\rm CO})[{\rm cm}^{-2}] = 2.42\times10^{14} \times \frac{T_{\rm ex}}{1 - \exp(-5.29/T_{\rm ex})} \int {}^{13}\tau_i(\nu)\, d\nu. \quad (6)$$

Therefore, the total column density of ^{13}CO emission is given by

$$N_{\rm total}(^{13}{\rm CO})\,[{\rm cm}^{-2}] = 2.42\times10^{14} \frac{T_{\rm ex}\Delta V\, ^{13}\tau_0}{1 - \exp(-5.29/T_{\rm ex})}, \quad (7)$$

where ΔV is the approximate equivalent of the full velocity width at half maximum intensity and $^{13}\tau_0$ is the ^{13}CO optical depth at the line center. Therefore, the total LTE gas mass ($M_\odot$) can be determined using the following relation

$$M_{\rm LTE}\,[M_\odot] \simeq \mu_{\rm H_2}\, m_{\rm H} X({\rm H_2}/^{13}{\rm CO}) \sum_{\rm surface} N_{\rm total}(^{13}{\rm CO}), \quad (8)$$

where $\mu_{\rm H_2}\, m_{\rm H}$ denotes the mean molecular mass per H_2 molecule and $X({\rm H_2}\,/\,^{13}{\rm CO})$ represents the ratio of H_2 to ^{13}CO abundance. We used $\mu_{\rm H_2} = 2.72$ to take helium into account. $X({\rm H_2}\,/\,^{13}{\rm CO})$ is assumed as (Dickman 1978)

$$X({\rm H_2}\,/\,^{13}{\rm CO}) = 6\times10^5. \quad (9)$$

The distance to GF 6 was taken as approximately 190 pc from Maheswar & Bhatt (2006). In Table 2, we give the results of the LTE analysis of the eight subclumps identified in this paper. We treated each subclump as a uniform sphere for convenience and assigned a geometric center to each subclump. We fitted the observed profile of the column density to a Gaussian function of the form

$$N(^{13}{\rm CO}; p) = N_0\, \exp\left[-\left(\frac{p}{\sigma_r}\right)^2\right], \quad (10)$$

where N_0 means the central column density and p means the projected distance from the center of each subclump, and define the size of a subclump by the e-folding width σ_r of the best-fit Gaussian function. The radius of each clump was determined as an equivalent uniform sphere, which has the radius of a circle whose area is equal to the area within the half intensity contour.

Column (2) lists the column densities of ^{13}CO (J=1–0) toward the center of each clump. In Column (3), the total LTE gas masses derived with Equation (8) are listed. Columns (4) and (5) give the angular sizes in arcminute and the radii in parsec, respectively.

Each subclump may undergo an overall systematic motion, either collapse or expansion, and may simultaneously experience a certain amount of turbulent motion. If the turbulent velocity is much less than the systematic velocity, the line width near the cloud boundary will approach zero and the line width at the cloud center will reflect the systematic velocity. If the turbulent velocity is comparable to the systematic velocity, the line width at the cloud center will be some sort of weighted mean of both systematic and turbulent velocities, while the line width near the boundary would reflect the turbulent velocity only. In this respect, the observed line width dispersion is often decomposed into a systematic and turbulent part using Kim & Hong (2009)

$$\Delta V_{\rm obs}^2(p) \simeq \Delta V_{\rm sys}^2(p) + \Delta V_{\rm tur}^2\,. \quad (11)$$

The line width dispersion $\Delta V_{\rm obs}$ may not be directly derived from the observed profile for several reasons. In most cases, the observed profiles do not have an exact Gaussian shape but rather have an asymmetrical shape.

Table 2 Derived Physical Properties of Eight Subclumps

Subclump	$N(^{13}\mathrm{CO})$ (10^{16} cm^{-2})	$M^a_{\rm LTE}$ ($M_\odot$)	$\sigma_{\rm r}$ (arcmin)	R^a (pc)	$\Delta V_{\rm obs}(p=0)$ (km s^{-1})	$\Delta V_{\rm tur}$ (km s^{-1})	$\Delta V_{\rm FWHM}$ (km s^{-1})	$M_{\rm VIR}$ ($M_\odot$)
(1)	(2)	(3)	(4)	(5)	(6)	(7)	(8)	(9)
GF 6-a	2.61	1.04	1.97±0.37	0.11±0.02	0.79±0.10	0.50±0.07	0.44±0.05	4.44±2.01
GF 6-b	9.12	3.64	2.78±0.26	0.15±0.02	0.94±0.11	0.59±0.07	0.52±0.05	8.52±3.13
GF 6-c	5.90	2.36	2.45±0.27	0.14±0.01	0.78±0.07	0.49±0.04	0.43±0.05	5.48±1.68
GF 6-d	7.42	2.96	2.26±0.23	0.13±0.01	1.02±0.07	0.64±0.04	0.56±0.05	8.69±2.25
GF 6-e	7.46	2.98	2.34±0.29	0.13±0.02	1.01±0.08	0.64±0.05	0.56±0.05	8.59±3.08
GF 6-f	4.06	1.62	1.66±0.16	0.09±0.01	0.85±0.05	0.53±0.03	0.47±0.03	4.16±1.12
GF 6-g	6.72	2.68	3.12±0.40	0.17±0.02	0.54±0.05	0.34±0.03	0.30±0.03	3.19±1.13
GF 6-h	3.74	1.50	2.13±0.28	0.12±0.02	0.93±0.10	0.58±0.06	0.51±0.05	6.64±2.59

Notes: ^{a} The size and mass are based on the distance of 190 pc.

The observed lines, of course, show spiky features due to noise. Furthermore, due to optical saturation, the line is broadened with respect to the Gaussian as the optical depth increases. We thus corrected the observed profiles for the effects of asymmetric shape, noise and optical saturation. The results of $\Delta V_{\rm obs}$ at the center $(p = 0)$ of each subclump and $\Delta V_{\rm tur}$ are listed in Columns (6) and (7) of Table 2, respectively. We use these values in the next section of the stability analysis.

2.4 Stability Analysis

For a more detailed discussion of the dynamical state and the evolution of this cloud, we performed stability analysis using the simple scalar virial theorem. The virial theorem is a useful tool for describing an overall energy balance and checking the question of stability. For the stability analysis, the virial theorem without the moment of inertia term has been widely used due to its simplicity. As discussed by many authors (see Spitzer 1978), several energy terms, including turbulence and systematic motion, magnetic field, gravitational potential and external pressure, must sum to zero to be a steady state. In practice, it is difficult to determine all the terms accurately because of the unknown internal structures and the irregular shape of interstellar clouds. Kim & Hong (2009) analyzed the stability of 12 small dark globules by using the scalar virial theorem. We have also applied and analyzed using the same theorem. Details were summarized in Kim & Hong (2009).

Assuming that most subclumps of GF 6 have the shape of a globule, we take a spherical geometry for the shape and replace the structure by uniform distributions of density, temperature and turbulence dispersion. In this case, for a uniform cloud of mass M and radius R, we can express a simple type of the virial theorem as

$$4\pi R^3 P_{\rm ext} = M \left\langle V^2_{\rm tur} \right\rangle - \frac{3\,GM^2}{5\,R}, \qquad (12)$$

where $V_{\rm tur}$ is the rms turbulent velocity and $P_{\rm ext}$ is a uniform external pressure (Leung et al. 1982). If we may ignore the external pressure term, the simplest version of the scalar virial theorem in the stability analysis becomes

$$\left\langle V^2_{\rm tur} \right\rangle \simeq \frac{3\,GM}{5\,R}. \qquad (13)$$

As Langer et al. (1989) described, we can only observe the line of sight velocity and the separation of two points perpendicular to the line of sight. Assuming equipartition among the three velocity components,

$$\left\langle V^2_{\rm tur} \right\rangle = \left\langle V^2_{x,{\rm tur}} \right\rangle + \left\langle V^2_{y,{\rm tur}} \right\rangle + \left\langle V^2_{z,{\rm tur}} \right\rangle, \qquad (14)$$

and if we assume that the observed line is perfectly Gaussian, the turbulent velocity is directly proportional to the full width at half maximum ($\Delta V_{\rm FWHM}$) with a factor of $2\sqrt{2\ln 2}$;

$$\begin{aligned} \left\langle V^2_{\rm tur} \right\rangle &= 3 \left\langle V^2_{z,{\rm tur}} \right\rangle \simeq 3 \left(\frac{\Delta V_{\rm FWHM}}{2\sqrt{2\ln 2}} \right)^2 \\ &= 0.541\, \Delta V^2_{\rm FWHM}, \end{aligned} \qquad (15)$$

where $V_{z,{\rm tur}}$ is the line of sight component of turbulent velocity. Utilizing Equation (15), Equation (13) can be rewritten as

$$\begin{aligned} \Delta V_{\rm FWHM}[{\rm km\ s^{-1}}] &\simeq \left\{ \left(\frac{4.302 \times 10^{-3}}{0.541} \right) \left(\frac{3{\rm M}}{5{\rm R}} \right) \right. \\ &\left. \left[\frac{\rm pc}{M_\odot} \right] \right\}^{1/2} = 6.907 \times 10^{-2} \left[\frac{M}{M_\odot} \frac{\rm pc}{R} \right]^{1/2}. \end{aligned} \qquad (16)$$

Leung et al. (1982) and Kim & Hong (2009) compared the observed ^{13}CO line width ΔV with $(M_{\rm LTE}/R)^{1/2}$

for their sample of dark clouds. Assuming that all subclumps of GF 6 are isolated, our analysis has progressed via a similar method. As we discussed in Section 2.3, the core part of subclumps undergoes a systematic expansion or contraction, and near the boundary undergoes only spatially varying turbulence dispersion. We thus take the mean velocity dispersion $\langle\sigma(\Delta V)\rangle$ and can obtain from observable quantities as

$$\langle\sigma(\Delta V)\rangle = [\Delta V_{\rm obs}(p=0) + \Delta V_{\rm tur}]/2. \qquad (17)$$

This relation between $\langle\sigma(\Delta V)\rangle$ and $(M_{\rm LTE}/R)^{1/2}$ is shown in Figure 4, where two solid lines represent $\pm$ 30% deviations from the virial equilibrium for the effects of finite opacity and different degrees of central concentration in the gas density distribution. Taking into account the error value, the subclumps lying within solid lines are said to be in virial equilibrium. The subclumps lying on the upper side of this equilibrium band will expand, while those on the lower side should be gravitationally bound or may even undergo significant gravitational contraction. As shown in Figure 4, we can guess that most subclumps will expand and that only GF 6-g is approximately in virial equilibrium.

To support the result of the stability analysis more firmly, we present another stability test based on the relation between the LTE mass and the virial mass. The virial mass is derived from Equation (16) as

$$M_{\rm vir}\,[M_\odot] \simeq 210 \left[\frac{R}{\rm pc}\right]\left[\frac{\Delta V_{\rm FWHM}}{\rm km\ s^{-1}}\right]^2, \qquad (18)$$

assuming spherical shape and uniform density. According to what is dealt with in Section 2.3 and Equations (15)–(17),

$$\Delta V_{\rm FWHM}\,[\rm km\ s^{-1}] = \frac{1}{2}\left[\frac{8\ln 2}{3}\right]^{1/2}\langle\sigma(\Delta V)\rangle \simeq 0.68\,\langle\sigma(\Delta V)\rangle\,. \qquad (19)$$

Checking these relations, we can interpret if each subclump of GF 6 is in a state of virial equilibrium or if they are expanding or gravitationally collapsing. Derived $\Delta V_{\rm FWHM}$ and virial masses for each subclump are listed in Columns (8) and (9) of Table 2.

Figure 5 shows the relation between the LTE mass, $M_{\rm LTE}$, and the virial mass, $M_{\rm vir}$, at the logarithmic scale for the eight subclumps. For the filled circles, we attached error bars, taking into account the size and turbulence dispersion. The dashed line represents the location of strict virial equilibrium. The results agree well with those of the previous test, i.e. only GF 6-g is approximately in virial equilibrium. However, there are various uncertainties in the LTE and virial mass estimation: the uncertainty of the relative abundance of ^{13}CO to H_2, uncertainties in the shape and density structure of the clump and uncertainties in the size of the clumps and the turbulence dispersion. This error estimation would systematically underestimate or overestimate the masses derived using the LTE and virial techniques. Given generally accepted uncertainties, errors of a factor of two could be at least considered in one or the other of the mass estimates.

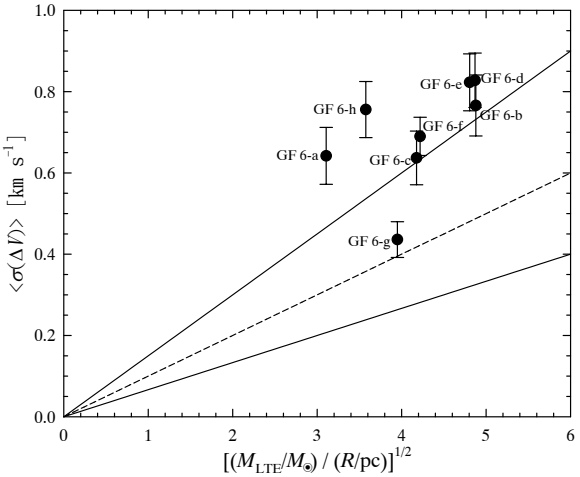

Fig. 4 The mean velocity dispersions of the observed ^{13}CO line are plotted as a function of $(M_{\rm LTE}/R)^{1/2}$ for the eight subclumps of GF 6. See the main text for an additional description.

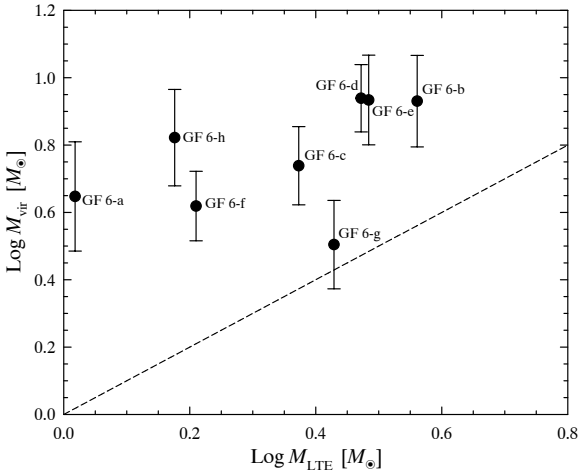

Fig. 5 The relation between the LTE mass, $M_{\rm LTE}$, and the virial mass, $M_{\rm vir}$, at the logarithmic scale for the eight subclumps of GF 6. See the main text for the detailed description.

3 INFRARED PROPERTIES

3.1 Mid- and Far-infrared Data

Data from the *IRAS* survey were HIRES-processed at the Infrared Processing and Analysis Center (IPAC), Caltech, to obtain high angular resolution maps for the region around GF 6. *HIgh RESolution* (HIRES) employs the Maximum Correlation Method (MCM) to construct (resolution-enhanced) co-added images; the HIRES program is also known as YORIC. Information regarding the MCM can be found in Aumann et al. (1990) and Cao et al. (1996). There is HIRES documentation available on the web (*http://irsa.ipac.caltech.edu/IRASdocs/hires_over.html*) and in the IPAC User's Guide.

The HIRES image was obtained in the size of $1^\circ \times 1^\circ$, with a pixel size of $15''$ and default processing. The data were de-striped via detector baseline removal, and flux bias (any overall slope to the field, e.g., from zodiacal light) was removed. A second pass de-striper, the offset compensation de-striper, was applied to remove residual stripe. Beam sample maps used a regular grid of 10 Jy sources on a smoothed background. The algorithm was iterated 20 times, with maps produced at the 1st, 5th, 10th and 20th iterations. To see detailed dust emission, we examined the map of the 20th iteration in the four bands (12, 25, 60 and 100 μm).

Point sources were selected from the *IRAS* Point Source Catalog for the area around the GF 6 region. We also added the mid-infrared (MIR) data from the *MSX* Point Source Catalog to find correlations between far-infrared (FIR) point sources and MIR point sources.

3.2 Infrared Properties

We examined both the FIR and MIR point sources detected based on *IRAS* and *MSX* toward the GF 6 region. The data were used to investigate dust properties of this region and to search whether GF 6 contains embedded young stellar objects.

The ^{13}CO (J=1–0) contour maps overlaid on the HIRES-processed *IRAS* images in the 60 and 100 μm bands are shown in Figure 6. The region mapped in ^{13}CO (J=1–0) is represented by the solid line, while the six *IRAS* point sources in the vicinity of the GF 6 region are represented by green crosses. We find that core parts of the ^{13}CO map, namely GF 6-a, b, d and e, correspond somewhat well with the cores of the *IRAS* 100 μm map. The infrared parameters of these six *IRAS* point sources are presented in Table 3. It includes the *IRAS* names, equatorial coordinates and flux densities at the four wavelength bands. Moreover, listed error values of the flux densities are the corresponding error or uncertainty in measurements (see IRAS Explanatory Supplement, 1988).

In Columns (8) and (9) of Table 3, we give the derived FIR luminosities of selected *IRAS* sources according to the method of Lonsdale & Helou (1985) and give the associated subclump names, respectively. Among the six *IRAS* point sources, four sources are located outside the boundary of the region. These four sources may be background or foreground objects unassociated with GF 6 because they have spectra characteristic of normal stars, as presented in Table 3. Normal stars are mainly detected at 12 and 25 μm, showing flux densities satisfying $S_{12} > S_{25}$ (Clemens & Barvainis 1988). Two out of six *IRAS* point sources lie within the boundary of the region and seem to be associated with two subclumps, i.e., GF 6-d and GF 6-e, respectively. These two *IRAS* sources, i.e. IRAS 18588−0530 and IRAS 18593−0535, have FIR luminosities of 0.15 $L_\odot$. This value is more consistent with infrared cirrus than with generally known young stellar objects (Weiland et al. 1986).

To better see whether these infrared point sources are associated with any embedded young stellar objects, we also investigate the relation between FIR point sources with *IRAS* data and MIR point sources with *MSX* data. The parameters of the *MSX* sources are presented in Table 4. Column (6) of Table 4 lists subclumps or *IRAS* sources that seem to be associated with *MSX* sources.

Figure 7 shows both the *IRAS* and *MSX* point sources on the ^{13}CO integrated intensity map, overlaid on the *IRAS* flux image at 100 μm. We found that 10 *MSX* point sources lie near the GF 6 region. It seems that three out of 10 *MSX* point sources lie within the boundary of the ^{13}CO map and one of three *MSX* sources is associated with the subclump GF 6-e or IRAS 18593−0535 within a $1'$ radius. However, all three sources were detected under 1 Jy at only the 8.28 μm band. The remaining seven sources lie on the edge or outside the CO boundary of the region.

Because this investigation of the relation between *IRAS* and *MSX* point sources on the ^{13}CO map is not clear, it remains inconclusive. Therefore, for the *IRAS* sources near the GF 6 region (see Table 3), we adopt the empirical approach of plotting the distribution of these sources in the *IRAS* two-color diagram. The two *IRAS*

Table 3 *IRAS* Point Sources Associated with the GF 6 Region

IRAS name	R.A. (J2000) (h m s)	Dec. (J2000) (d m s)	S_{12} (Jy)	S_{25} (Jy)	S_{60} (Jy)	S_{100} (Jy)	$L_{\rm FIR}$ ($L_\odot$)	Subclump name
(1)	(2)	(3)	(4)	(5)	(6)	(7)	(8)	(9)
18587−0534	19 01 25.2	−05 29 40	13.95±1.26	8.49±0.59	1.79±0.14	< 30.60	0.50	···
18588−0530	19 01 32.5	−05 26 35	< 0.53	< 0.46	1.16±0.13	7.71±1.08	0.15	GF 6-d
18590−0539	19 01 40.2	−05 35 29	0.57±0.05	< 0.25	< 0.56	< 32.40	0.48	···
18593−0535	19 01 58.3	−05 31 33	< 0.81	< 0.39	1.07±0.10	< 7.88	0.15	GF 6-e
18594−0519	19 02 08.3	−05 14 39	< 0.53	< 0.28	0.79±0.10	< 19.20	0.30	···
18598−0522	19 02 31.0	−05 18 08	1.61±0.11	1.22±0.27	< 0.69	< 28.60	0.43	···

Notes: S_{12}, S_{25}, S_{60} and S_{100} indicate flux densities at the four *IRAS* wavelength bands.

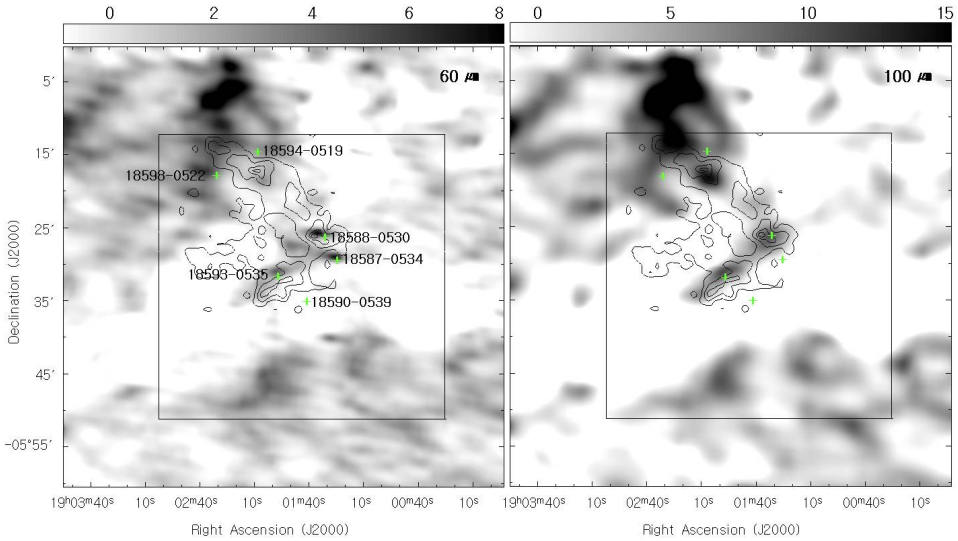

Fig. 6 ^{13}CO (J=1–0) integrated intensity contours overlaid on HIRES-processed 60 and 100 μm *IRAS* images. *IRAS* point sources are marked with *green crosses*.

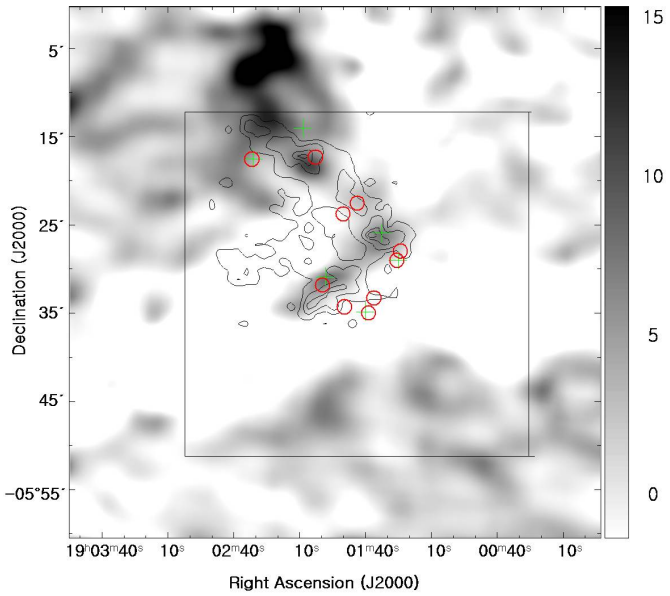

Fig. 7 *IRAS* and *MSX* point sources on the ^{13}CO integrated intensity map, overlaid on the *IRAS* flux image at 100 μm. *Green crosses* indicate the *IRAS* point sources and *red open circles* indicate the *MSX* point sources.

Table 4 *MSX* Point Sources Associated with the GF 6 Region

MSX name	A (8.28 μm) (Jy)	C (12.13 μm) (Jy)	D (14.65 μm) (Jy)	E (21.34 μm) (Jy)	Subclump, *IRAS* name
(1)	(2)	(3)	(4)	(5)	(6)
G029.1796−04.7052	0.65±0.03	< 1.69	< 0.94	···	···
G029.1672−04.7190	21.16±0.87	21.16±1.06	14.03±0.86	13.05±0.80	18587−0534
G029.1233−04.7901	0.30±0.02	···	···	···	···
G029.1031−04.8120	0.66±0.03	···	···	···	18590−0539
G029.2977−04.7364	0.22±0.01	···	···	···	GF 6-c
G029.1342−04.8476	0.25±0.02	···	< 0.82	···	···
G029.2918−04.7692	0.21±0.01	···	···	···	···
G029.1897−04.8654	0.53±0.02	···	···	···	GF 6-e, 18593−0535
G029.4118−04.7673	0.30±0.02	···	···	···	GF 6-b
G029.4632−04.8758	2.02±0.08	1.93±0.14	1.48±0.12	···	18598−0522

colors are defined as $[S_{25} - S_{12}] = \log(S_{25}/S_{12})$ and $[S_{60} - S_{25}] = \log(S_{60}/S_{25})$.

Figure 8 shows the *IRAS* two-color diagram as a plot of $[S_{25} - S_{12}]$ versus $[S_{60} - S_{25}]$ for all sources in Table 3. Also marked in Figure 8 are the regions in which normal stars (giant or supergiant stars surrounded by circumstellar dust shells; dashed area), bulge stars (evolved late type M stars; solid area) and T-Tauri stars (dotted area) are found (Emerson 1987; Harris et al. 1988). The two-color diagram suggests that two sources, i.e., IRAS 18587−0534 and IRAS 18598−0522, have similar *IRAS* colors as those of normal stars and bulge stars. For completeness, we searched catalogs with variable stars and found these sources from the catalog of MISAO new variable stars (Yoshida & Kadota 1999). IRAS 18587−0534 is a variable star with Max. CCD magnitude = 10.9 and Min. CCD magnitude = 12.7. IRAS 18598−0522 is also a variable star with Max. CCD magnitude = 12.0 and Min. CCD magnitude = 13.7. These two sources are located outside the CO boundary and do not show any definite relationship with the GF 6 region. The remaining four sources are located in the mid-rightward area of the two-color diagram (Figure 8) and have *IRAS* colors more or less coincident with the infrared cirrus (Low et al. 1984; Weiland et al. 1986). They defined diffuse filamentary dust clouds that show conspicuous thermal emission at the 100 μm band as the infrared cirrus. Emerson (1987) designated 160 sources out of 1099 *IRAS* sources, that were seen towards southern dark clouds, as having "cirrus colors," defined as a detection only at 100 μm (91 sources) or detection at 60 and 100 μm with $[S_{100} - S_{60}] > +0.6$ (69 sources). He also demonstrated that the cirrus clearly appeared from the strong peak at $[S_{100} - S_{60}] = +0.8$ in the histogram of number of detections at $[S_{100} - S_{60}]$. Two *IRAS* sources, i.e., IRAS 18588−0530 and IRAS 18593−0535, which lie toward GF 6-d and GF 6-e, are objects of concern and have values of 0.82 and 0.87 at $[S_{100} - S_{60}]$, respectively. These two sources predominantly have colors of the infrared cirrus feature.

To identify the dust components of two *IRAS* sources, i.e., IRAS 18588−0530 and IRAS 18593−0535 as cirrus clumps, we calculate a dust color temperature, which is derived from the integrated flux density ratio at 60 and 100 μm, assuming that the dust in a single beam can be characterized by one temperature ($T_{\rm d}$) and that the sources have spectra that can be represented by black bodies modified by an extinction law (Arce & Goodman 1999). If the dust color temperature, $T_{\rm d}$, at 60 and 100 μm satisfies $\exp\left[hc\,/\lambda k T_{\rm d}\right] \gg 1$, the color temperature is given by

$$T_{\rm d} \simeq \frac{hc/k\,(1/\lambda_{60} - 1/\lambda_{100})}{(3+\beta)\ln(\lambda_{100}/\lambda_{60}) + \ln(S_{100}/S_{60})}, \quad (20)$$

where S is the flux density at a given wavelength and β is the emissivity index. The dust grain emissivity, ε, has been assumed to follow the power law $\varepsilon \propto \lambda^{-\beta}$. Although the emissivity index, β, is hard to estimate and studies differ in the value they find for β, there is a general agreement that β depends on the grain's size, composition and physical structure (Weintraub et al. 1991). The general consensus has been that β has a value most likely between 0 and 2, with $\beta = 1$ or $\beta = 2$ favored by various groups. $\beta = 1$ has mainly been applied for 50 μm $\leq \lambda \leq$250 μm and $\beta = 2$ for $\lambda >$250 μm (Hildebrand 1983; Wu & Evans 1989). Meanwhile, Cox & Mezger (1989) suggested that the total absorption cross section of the graphite-silicate mixture at FIR wavelengths can be well approximated with $\beta = 1.5$ for 40 μm $\leq \lambda \leq$ 100 μm, and $\beta = 2$ for $\lambda >$100 μm.

To make a coherent comparison with previous studies of similar samples (Clemens & Barvainis 1988; Carpenter et al. 1990; Lee & Lee 2005), we adopt the

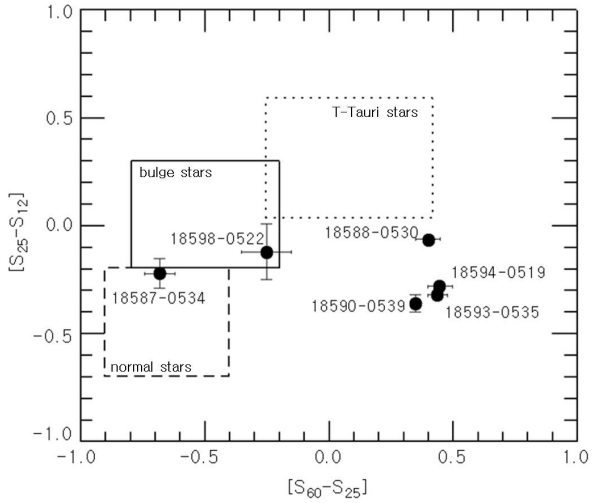

Fig. 8 The $[S_{25} - S_{12}]$ versus $[S_{60} - S_{25}]$ color-color diagram for *IRAS* point sources associated with the GF 6 region. The regions occupied by normal stars (giant or supergiant stars surrounded by circumstellar dust shells; *dashed area*), bulge stars (evolved late type M stars; *solid area*) and T-Tauri stars (*dotted area*) are shown for reference.

Table 5 Infrared Properties of Two *IRAS* Sources within the Boundary of the GF 6 Region

IRAS name	$[S_{25} - S_{12}]$	$[S_{60} - S_{25}]$	$[S_{100} - S_{60}]$	S_{60}/S_{100}	$T_{\rm d}\,(\beta = 1)$ (K)	$T_{\rm d}\,(\beta = 1.5)$ (K)
(1)	(2)	(3)	(4)	(5)	(6)	(7)
18588−0530	−0.06	0.40±0.05	0.82±0.11	0.15	24.4±1.4	22.9±1.5
18593−0535	−0.32	0.44±0.04	0.87±0.04	0.14	23.7±0.8	22.3±0.5

values $\beta = 1$ and $\beta = 1.5$ for our sources. The resulting dust color temperatures of two *IRAS* sources are listed in Table 5. Columns (2)–(4) give the *IRAS* color-color indices at each wavelength. In Column (5), S_{60}/S_{100} represents the integrated flux density ratio of 60 μm to 100 μm, while Columns (6) and (7), i.e., $T_{\rm d}\,(\beta = 1)$ and $T_{\rm d}\,(\beta = 1.5)$, represent the dust color temperatures at the values $\beta = 1$ and 1.5, respectively. The ratios of the 60 μm to the 100 μm integrated flux density for two *IRAS* sources are 0.15 and 0.14, and the dust color temperatures for the value $\beta = 1$ are 24.4 K and 23.7 K, while the dust color temperatures for the value $\beta = 1.5$ are 22.9 K and 22.3 K, respectively. Molecular clouds with active star formation have an S_{60}/S_{100} ratio of 0.43 – 0.78 and a dust color temperature of $\sim$ 37 K (Carpenter et al. 1990). On the other hand, the molecular clouds that have the colder dust color are considered to be infrared cirrus. The S_{60}/S_{100} ratio of these clouds is 0.12 – 0.18 and corresponds to the dust color temperature of 22 – 24 K (Blitz et al. 1984; Weiland et al. 1986; Snell et al. 1989). According to these comparisons, the GF 6 region is similar to an infrared cirrus rather than a star forming region. The dust heating of this region can probably be explained as being heated by the interstellar radiation field (ISRF) rather than heated by an embedded young stellar source. Several authors have computed models of thermal emission from dust grains heated by the ISRF (Kruegel & Walmsley 1984; Draine & Anderson 1985; de Muizon & Rouan 1985). They found that smaller particles are heated more easily and that graphite grains probably predominate among them. The observed "hot" dust will then be mainly graphite and the "cold" dust will be silicate. It is known that the mean temperature of grains exposed to the ISRF is 10 K for silicate grains and 20 K for graphite grains.

4 SUMMARY AND CONCLUSIONS

To investigate the internal structure and evolutionary state of a filamentary cloud GF 6, we carried out both molecular line observations and infrared data analysis using *IRAS* and *MSX* data. For the radio observations, we performed mapping observations of ^{12}CO (J=1–0) and ^{13}CO (J=1–0) emission lines. Using the derived physical properties of GF 6, we performed virial stability tests. For most subclumps, the virial masses are 3 or 4 times larger than the LTE ones. This result suggests that most

subclumps in GF 6 will expand and eventually be dissipated away.

By analyzing the infrared archived data of *IRAS* and *MSX*, we identified two infrared point sources, i.e. IRAS 18588−0530 and IRAS 18593−0535, which seem to be associated with the GF 6 region. We examined the infrared properties for these two *IRAS* point sources regarding whether they are newly formed young stellar objects. The flux density ratios at 100 and 60 μm, i.e., $[S_{100} - S_{60}]$, of the two *IRAS* sources are 0.82 and 0.87, respectively. These values are much higher than those obtained from a typical star forming cloud, and similar to those from infrared cirrus. The low dust color temperature, 22–24 K, from these *IRAS* point sources also supports the consideration that these are infrared cirrus.

Both radio and infrared properties, together with the lack of clear evidence of star formation, suggest that GF 6 is an infrared cirrus rather than star forming cloud. The dust heating of this region is probably due to the ISRF rather than an embedded young stellar object.

Acknowledgements This work was partly sponsored by the 100 Talents Project of the Chinese Academy of Sciences, the National Natural Science Foundation of China under grant 11673051 and the Natural Science Foundation of Shanghai under grant 15ZR1446900. This research utilized data products from the Midcourse Space Experiment and Infrared Astronomical Satellite; the NASA/IPAC Infrared Science Archive, which is operated by the Jet Propulsion Laboratory, California Institute of Technology, under contract with the National Aeronautics and Space Administration.

References

André, P., Di Francesco, J., Ward-Thompson, D., et al. 2014, Protostars and Planets VI, 27 (arXiv:1312.6232)
Arce, H. G., & Goodman, A. A. 1999, ApJ, 517, 264
Aumann, H. H., Fowler, J. W., & Melnyk, M. 1990, AJ, 99, 1674
Barnard, E. E. 1927, A Photographic Atlas of Selected Regions of the Milky Way (Carnegie Institution of Washington)
Benson, P. J., & Myers, P. C. 1989, ApJS, 71, 89
Blitz, L., Magnani, L., & Mundy, L. 1984, ApJ, 282, L9
Bok, B. J., & Reilly, E. F. 1947, ApJ, 105, 255
Cao, Y., Prince, T. A., Terebey, S., & Beichman, C. A. 1996, PASP, 108, 535
Carpenter, J. M., Snell, R. L., & Schloerb, F. P. 1990, ApJ, 362, 147
Clemens, D. P., & Barvainis, R. 1988, ApJS, 68, 257
Cox, P., & Mezger, P. G. 1989, A&A Rev., 1, 49
de Muizon, M. J., & Rouan, D. 1985, A&A, 143, 160
di Francesco, J., Evans, II, N. J., Caselli, P., et al. 2007, in Protostars and Planets V., eds., B. Reipurth, D. Jewitt, & K. Keil (Tucson: Univ. Arizona Press), 17
Dickman, R. L. 1978, ApJS, 37, 407
Draine, B. T., & Anderson, N. 1985, ApJ, 292, 494
Emerson, J. P. 1987, in IAU Symposium, 115, Star Forming Regions, ed. M. Peimbert & J. Jugaku, 19
Haikala, L. K., & Reipurth, B. 2010, A&A, 510, A1
Haikala, L. K., & Reipurth, B. 2017, A&A, 597, A118
Harris, S., Clegg, P., & Hughes, J. 1988, MNRAS, 235, 441
Heigl, S., Burkert, A., & Hacar, A. 2016, MNRAS, 463, 4301
Hildebrand, R. H. 1983, QJRAS, 24, 267
Keto, E., & Burkert, A. 2014, MNRAS, 441, 1468
Kim, B. G., & Jung, J. H. 1992, Publication of Korean Astronomical Society, 7, 149
Kim, H. G., & Hong, S. S. 2002, ApJ, 567, 376
Kim, H. G., & Hong, S. S. 2009, New Astron., 14, 451
Kirk, J. M., Ward-Thompson, D., & André, P. 2005, MNRAS, 360, 1506
Kruegel, E., & Walmsley, C. M. 1984, A&A, 130, 5
Kutner, M. L., & Ulich, B. L. 1981, ApJ, 250, 341
Langer, W. D., Wilson, R. W., Goldsmith, P. F., & Beichman, C. A. 1989, ApJ, 337, 355
Larson, R. B. 1985, MNRAS, 214, 379
Lee, Y., & Lee, C. W. 2005, New Astron., 10, 463
Lehtinen, K., Mattila, K., & Lemke, D. 2005, A&A, 437, 159
Leung, C. M., Kutner, M. L., & Mead, K. N. 1982, ApJ, 262, 583
Lonsdale, C. J., & Helou, G. 1985, , Catalogued Galaxies and Quasars Observed in the *IRAS* Surve, Pasadena: Jet Propulsion Laboratory (JPL), 1985
Low, F. J., Young, E., Beintema, D. A., et al. 1984, ApJ, 278, L19
Lynds, B. T. 1962, ApJS, 7, 1
Maheswar, G., & Bhatt, H. C. 2006, MNRAS, 369, 1822
Moreira, M. C., & Yun, J. L. 2002, A&A, 381, 628
Roh, D.-G., & Jung, J. H. 1999, Publication of Korean Astronomical Society, 14, 123
Samal, M. R., Pandey, A. K., Ojha, D. K., et al. 2007, ApJ, 671, 555
Schneider, S., & Elmegreen, B. G. 1979, ApJS, 41, 87
Snell, R. L., Schloerb, F. P., & Heyer, M. H. 1989, ApJ, 337, 739
Spitzer, L. 1978, Physical Processes in the Interstellar Medium (New York: Wiley-Interscience)
Stutz, A., Launhardt, R., Linz, H., et al. 2010, A&A, 518, L87
Weiland, J. L., Blitz, L., Dwek, E., et al. 1986, ApJ, 306, L101
Weintraub, D. A., Sandell, G., & Duncan, W. D. 1991, ApJ, 382, 270
Wu, Y., & Evans, II, N. J. 1989, ApJ, 340, 307
Yoshida, S., & Kadota, K. 1999, Information Bulletin on Variable Stars, 4746
Yun, J. L., & Clemens, D. P. 1990, ApJ, 365, L73